Measurement of the electronic momentum distributions of Rydberg Stark states

J. Murray-Krezan and R. R. Jones
Department of Physics, University of Virginia, Charlottesville, Virginia 22904-4714, USA
(Received 2 December 2006; revised manuscript received 6 March 2007; published 8 June 2007)

Approximate momentum distributions of Rydberg electrons in static electric fields have been obtained using an improved impulsive momentum retrieval (IMR) technique. An imaging detector enables the measurement of half-cycle pulse (HCP) ionization probability across the spatial profile of a focused half-cycle pulse beam. By modulating the HCP amplitude we directly measure the derivative of the ionization vs HCP impulse curve, enabling the recovery of momentum distributions with better resolution than previously demonstrated with IMR. For example, for Stark states with small dipole moments, we observe predicted fine-structure in the projection of the momentum distribution along the Stark field axis. We use a semiclassical model to simulate the effect that the nonzero HCP duration has on our measurements. Good agreement between simulated and measured momentum distributions is obtained.

DOI: 10.1103/PhysRevA.75.063411 PACS number(s): 32.80.Rm

Atomic ionization by impulsive kicks provides a time-resolved method to monitor the evolution of electron wavepackets. Indeed, in several experiments [1–8] nearly unipolar "half-cycle" electric field pulses (HCPs) have been used to probe time-dependent changes in the momentum space probability distributions of evolving wavepackets. A more complete view of electron motion is available through impulsive momentum retrieval (IMR), a technique that allows the recovery of the full electronic momentum distribution projected along any Cartesian axis [1,9–12]. In IMR, ionization probability, I, is measured as a function of HCP "kick" strength or impulse $\vec{A}=-\int\vec{F}_{\mathrm{HCP}}(t)dt$. Unless otherwise noted, atomic units are used throughout. In the instantaneous kick limit, the ionization probability $I(A)$ for a given electron binding energy $E(>0)$ and impulse A is equal to the probability that the electron's momentum in the kick direction exceeds a critical value [1,2,11]

$$p_c=\left(E-\frac{1}{2}A^2\right)\Big/A. \tag{1}$$

Therefore, the electron's momentum distribution along the kick axis, at the instant of the impulse

$$D(p)=\frac{dI}{dp}=\frac{dI}{dA}\left.\frac{dA}{dp_c}\right|_{p_c=p} \tag{2}$$

can be obtained using Eq. (1) and a measurement of dI/dA [1,11].

Since its introduction, IMR has been successfully applied to obtain approximate electronic momentum distributions of eigenstates and wavepackets, in the latter case providing a time-resolved view of coarse changes in the momentum distribution [1,9–11]. In principle, IMR is capable of resolving fine details of the momentum-space probability distribution, even nodal structure that reflects the quantum mechanical wave nature of the electron [12]. However, the full utility of IMR for measuring nuances of the probability distribution requires (i) a very short pulse and (ii) an accurate measurement of the slope of $I(A)$. As discussed further below, it is the electron acceleration distribution, not simply the ratio of the HCP duration to the characteristic electron period, that determines whether or not the short pulse criterion is met [9]. To satisfy the second criterion, we utilize an amplitude modulated HCP field to directly measure dI/dA [11]. We note that numerical differentiation of measured $I(A)$ curves greatly amplifies experimental noise, rendering this straightforward approach considerably less accurate.

Here we describe measurements of the momentum distributions of Rydberg Stark eigenstates [13,14] that serve as benchmarks for an improved amplitude modulated (AM) IMR technique. The experiments utilize an imaging detector and exploit the spatial variation in field strength across the HCP beam profile to simultaneously measure the HCP-ionization yield over a continuous range of impulses (see Fig. 1). The method eliminates the need for lengthy scans of HCP field strength, reducing errors associated with various experimental drifts. Though not explicitly demonstrated in the experiments described here, the technique can also be used for time-resolved measurements.

HCP ionization of Stark eigenstates has been studied previously [13,15–17]. These states provide useful benchmarks for exploring the effectiveness of electronic momentum measurement techniques. Indeed, Wetzels *et al.* [14] demonstrated a different electronic momentum recovery method on Rydberg Stark states in Xe. In their method, a short HCP ionizes a Rydberg electron, primarily affecting its momentum distribution in kick direction only. A velocity map imaging spectrometer is then used to measure the transverse momentum distribution of the continuum electron, and thereby infer the momentum distribution of the initial bound state. In that method, the momentum resolution and accuracy of the measurement are determined by the spectrometer resolution and the validity of the impulse approximation in the ionization step.

Stark eigenstates are useful for testing our AM-IMR method for several reasons. First, eigenstates have well-defined energies, so there is no "blurring" of the momentum distribution due to the uncertainty in the electron binding energy which is problematic in measurements of nonstationary states [1,12]. Second, direct comparison with theory is possible since the momentum-space wave functions are readily calculated from Coulomb wave functions $R(r)$ [18,19],

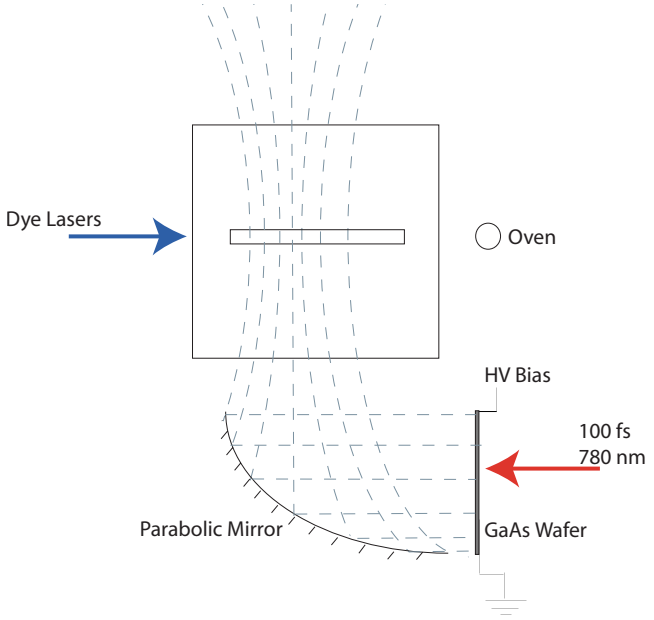

FIG. 1. (Color online) Schematic diagram of experiment (top view). The HCPs are produced by illuminating a high-voltage biased GaAs wafer. The HCP beam is focused across the beam of laser-excited Stark atoms beneath a slit in the upper of two parallel capacitor plates.

$$\Upsilon_{n,k,m}(p,\Theta,\Phi) = \sum_{n',l} (-i)^l a_{n,k,m;n',l,m} Y_{l,m}(\Theta,\Phi) \times \int_0^\infty r^2 R_{n',l}(r) j_l(pr) dr, \quad (3)$$

where $Y_{lm}(\Theta,\Phi)$ is a spherical harmonic function of angular coordinates in momentum space; j_l is a spherical Bessel function; $a_{n,k,m;n',l,m}$ is an admixture coefficient giving the angular momentum eigenstate amplitude in each Stark eigenstate; n, l, and m are the principal, angular momentum, and magnetic quantum numbers; and k is the parabolic quantum number which is proportional to the dipole moment $\langle z \rangle$ of the Stark state $k=2\langle z \rangle/3n$. In general, the $a_{n,k,m;n',l,m}$ can be computed by numerical diagonalization of the Stark+Coulomb Hamiltonian [20]. For hydrogenic systems, in weak static fields the eigenenergies shift linearly with the applied electric field F

$$E_{n,k} = -\frac{1}{2n^2} + \frac{3}{2}Fnk \quad (4)$$

and the $a_{n,k,m;n',l,m}$, which are non-negligible only if $n'=n$, can be expressed as Clebsch-Gordon coefficients [19,21]. Lastly, for $|k| \ll n$, the z projection of the electronic momentum distribution exhibits a small local minimum at its center. The visibility of this fine structure in the measured momentum distributions is a good indicator of the accuracy and resolution of the momentum retrieval method.

In the experiments, shown schematically in Fig. 1, two 5-ns dye lasers excite Ca atoms in a thermal beam from the $4s4s$ ground state, through a $4s4p$ intermediate level, into Stark eigenstates $4snk$, with $n=27$ or 28, $k=-n+|m|+1, -n+|m|+3, \ldots,$ or $n-|m|-3, n-|m|-1$, and magnetic quantum number $m=\pm 1$. The first dye laser pulse is polarized vertically ($\hat{z}$) and the second is polarized horizontally ($\hat{y}$). The atom and laser beams counter propagate along the $\hat{x}$ axis between two parallel aluminum plates that are separated by 2.0 cm. A constant voltage of 210 V is applied to the lower field plate, creating a static uniform electric field $\vec{F}=105$ V/cm $\hat{z}$ in the laser-atom interaction region. At this field strength, the Stark shifts of the $4s27k$ and $4s28k$ are approximately linear, the manifolds of Stark states associated with adjacent n levels do not overlap, and neighboring k states within the $n=27,28$ manifolds are separated by ~ 0.4 cm^{-1} [19]. The second dye laser, which has a bandwidth $\Delta\nu \simeq 0.15$ cm^{-1}, is frequency tuned to selectively populate individual Stark states. Given the linear Stark shifts and the fact that the numerically calculated admixture parameters $a_{n,k,m,n,l,m}$ are very similar to those for hydrogen [21], we label the states using hydrogenic $|nkm\rangle$ notation. However, unlike in hydrogen, $m=1$ electrons in Ca rapidly ionize at energies greater than the saddle-point energy in the combined Coulomb and static fields, $\epsilon=-2\sqrt{F}$. Therefore, when applying Eq. (1) in the momentum retrieval method, the appropriate binding energy is $E=-E_{n,k}+\epsilon$.

Approximately 20 ns after their creation, the Stark atoms are exposed to a HCP [22,23] whose duration $\tau_{\mathrm{HCP}}=0.5$ ps is much less than the classical Kepler period of the Rydberg electron $\tau_K=2\pi n^3$ (=2.99 and 3.34 ps at $n=27$ and 28, respectively). The HCP is polarized along the $\hat{z}$ axis and is generated by illuminating a biased 2 cm$\times$2 cm GaAs wafer with a 100 fs, 780 nm, ~ 40 μJ/cm^2 pulse from a Ti:Sapphire laser [22]. The peak electric field in the HCP is proportional to the bias voltage on the GaAs wafer. A parabolic mirror directs the HCP beam along the y axis, weakly focusing it to a ~ 1 cm waist at the intersection of the laser and atomic beams beneath the slit in the upper capacitor plate (see Fig. 1). The confocal parameter of the HCP beam is $\gg 1$ cm. Since the laser beam diameters (<0.1 cm) are much smaller than the diameter and confocal parameter of the HCP beam, there is negligible change in the HCP field across the lasers (i.e., in the yz plane). However, the HCP field varies from its maximum value to zero along the laser propagation axis ($\hat{x}$). Thus, Rydberg atoms at different locations along the slit experience different HCP impulses $\vec{A}(x)=-\int \vec{F}_{\mathrm{HCP}}(x,t)dt$. We exploit this position dependence to simultaneously measure the HCP ionization yield over a continuous range of HCP kick strengths.

Ions produced by the HCP are pushed by the static electric field through a narrow slit that lies along the x axis in the upper capacitor plate. Ions passing through the slit are projected onto an imaging detector consisting of a microchannel plate stack backed by a phosphor screen [24]. The position-dependent HCP ionization signal $I(x)$ is mapped onto the fluoresence intensity distribution on the phosphor screen and captured by a charged-coupled device (CCD) camera on each laser shot. The position-dependent impulse $A(x)$ is determined by measuring HCP ionization probability curves for Ca Rydberg d states as a function of x and GaAs bias voltage, and comparing these to previously calibrated ionization

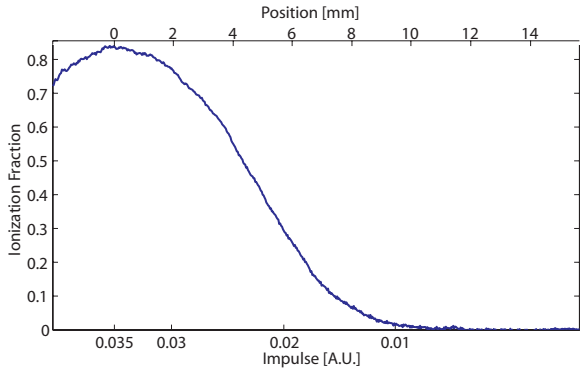

FIG. 2. (Color online) Spatial distribution of HCP ionization probability for $n=28$, $k=-26$ Ca atoms irradiated by roughly half of the transverse spatial profile of the HCP beam. The x-position axis (top) is relative to the HCP beam center (0 mm). The impulse axis (bottom) is calibrated using the variation in the on-axis ionization signal as the bias voltage on the GaAs wafer is scanned. The curve shown is the average result from seven laser shots.

vs impulse curves [9,25]. With this calibration, we can obtain an entire ionization versus HCP impulse curve $I(A)$ in a single laser shot, without scanning the wafer bias voltage (see Fig. 2).

The brief duration and predominant unipolar nature of the HCP are critical for implementing IMR. We utilize a second, unbiased GaAs wafer (W2) as a transient attenuator to confirm that the temporal characteristics of the HCP do not vary significantly across its beam profile [22,26]. For these tests, the HCP passes through W2 prior to entering the laser-atom interaction region. W2 is also illuminated by a time-delayed 100 fs, 780 nm laser pulse which serves as a fast shutter, decreasing the transmittance of W2 by roughly a factor of 10. The imaging detector is used to measure the ionization probability across the HCP beam profile as a function of the delay between the HCP and the shutter. We find that delay dependence of the ionization signal is essentially independent of transverse position within the beam.

Although $I(A)$ can be obtained in a single laser shot, an accurate derivative dI/dA is required to construct the desired momentum distribution $D(p_z)$ [see Eq. (2)]. Unfortunately, direct numerical differentiation of a measured ionization curve is problematic even with an excellent experimental signal to noise ratio. While data smoothing prior to differentiation can reduce the derivative noise levels significantly, it can also severely limit the achievable momentum resolution. Instead, we combine imaging detection with a HCP amplitude modulation technique [11] to measure the dI/dA curve with considerably higher accuracy. The basic AM-IMR method has been described in detail elsewhere [11]. In the current implementation, the spatially dependent ionization signal is measured as the impulse undergoes small oscillations about its nominal value $A(x,t)=A(x)(1+\alpha\cos 2\pi f_0 t)$, where $\alpha\simeq 0.01$ and $f_0=0.080$ Hz are the fractional modulation depth and the modulation frequency, respectively. The impulse modulation is achieved by adding a small ac component to the GaAs bias voltage. The precise value of f_0 is not critical. It is chosen to be much less than the 15 Hz laser repetition rate so that there are many laser shots per impulse modulation cycle. $I(x,t)$ is recorded over several thousand laser shots, converted to $I(A,t)$ and Fourier transformed with respect to time. The Fourier amplitude $I(A,f)$ evaluated at $f=f_0$ is immune to experimental noise at all other frequencies, and for $\alpha \ll 1$, is proportional to the desired curve dI/dA [11].

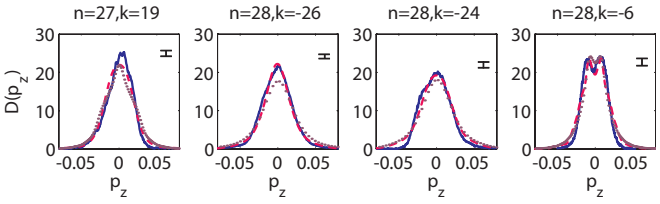

FIG. 3. (Color online) Measured (solid line) z-momentum distributions for various Stark eigenstates. Each curve represents the average of several measurements. The largest variance of the sample mean is shown as an error bar in each figure. The z projection of the momentum distributions calculated from Eq. (3) are shown as dotted curves. The results (dashed curves) of a numerical calculation (see text) of the expected momentum distributions $D(\bar{p}_z)$ retrieved using a 500 fs HCP are overlaid for comparison.

The accuracy and completeness of the momentum distributions is improved further by combining data sets acquired using positively and negatively polarized HCPs, respectively. The ionization probability curves produced with either polarity HCP rise from zero as the impulse is increased and asymptotically approach unity for very large impulses [13,23]. Consider a positive impulse $\vec{A}=A\hat{z}$. The initial rise of $I(A)$ is due to the ionization of electrons that have large, positive z momentum which contribute to the positive wing of the momentum distribution (see Fig. 3). The slow saturation of $I(A)$ for large impulses reflects the ionization of electrons with large, negative z momentum which represent the negative wing of the distribution. Thus, while the positive momentum half of the distribution can be obtained using relatively weak positive impulses for which $I(A)\leqslant 0.5$, recovery of the complete negative momentum portion of the distribution using positive impulses would require infinitely strong kicks [10,11]. Fortunately, with negative impulses, the negative momentum half of the distribution can be obtained using weak kicks for which $I(A)\leqslant 0.5$. Therefore, we circumvent the need for very strong pulses by constructing the positive and negative momentum halves of the distributions using relatively weak impulses $A_{\max}\sim\sqrt{2E}$ in the $\pm\hat{z}$ directions, respectively [10,11]. As discussed in more detail below, by avoiding the use of very strong impulses we also reduce errors associated with the noninstantaneous change in the electron's momentum in a real HCP and its affect on the motion of the electron in the Coulomb potential [9,27]. Each distribution is assembled from multiple measurements with oppositely polarized pulses, collected alternately in rapid succession (every few minutes) to minimize experimental drifts between runs. Good overlap of the two halves of the distributions near $p_z=0$ is obtained.

Figure 3 shows a set of experimentally determined momentum distributions. Each represents the average of several different data sets, collected on different days. In principle, the AM-IMR method ensures proper normalization of the

distributions $\int D(p_z)dp_z=1$, provided that α and f_0 are known, and the impulse at the 50% ionization point has been correctly calibrated. In practice, we find that the normalizations typically differ from unity by a few percent, due primarily to uncertainties in determining the precise signal magnitudes corresponding to 100% ionization in the impulse calibration scans. The amplitudes of the distributions in Fig. 3 have been individually adjusted (within a few %) to achieve unit normalization for better comparison between experimental and calculated results.

The distribution for the small dipole moment state $k=-6$ is the most distinct, with relatively small wings and a clear local minimum, or notch, at $p_z=0$. It is worth noting that this notch has a classical physics origin, however, a full description of the effect is beyond the scope of this paper [28]. The visibility of this notch indicates an experimental resolution of better than $\delta p \sim 0.005$ atomic momentum units, or $\sim 12\%$ of the full width at half maximum (FWHM) of the distribution. In our current apparatus, the best achievable resolution is approximately 5% of the distribution FWHM (~ 0.002 a.u. for $n=28$) due to the spatial resolution of the imaging spectrometer. Of course, the widths of the momentum distributions and the impulsive ionization curves scale as $\frac{1}{n}$ [13]. Thus, with an appropriately scaled maximum HCP field, our current apparatus affords a momentum resolution $0.05/n < \delta p < 0.15/n$ for Rydberg states with principal quantum number n. By comparison, the best reported resolution ($\delta p \sim 0.001$ a.u. at $n=34$) for Rydberg Stark state momentum measurements was achieved using HCP ionization followed by velocity map imaging detection [14]. That report, however, provides no explicit information on how (or if) this resolution scales with principal quantum number.

Two additional sets of curves are plotted with the experimental distributions in Fig. 3. The dotted lines show the theoretical momentum distributions, computed directly from the momentum space wave functions [see Eq. (3)]. The dashed curves are the results of a numerical calculation, described in more detail below, that uses a semiclassical approximation to simulate the effect of the nonzero HCP duration on the recovered momentum distributions. In general, the experimental curves are more sharply peaked than the "exact" theoretical curves, with greater amplitude near the center of the distribution and lower amplitude in the wings. This difference is particularly obvious for states $|k| \sim n$ which have large dipole moments and are preferentially aligned along the z axis. Apparently, the observed discrepancies are not caused by the finite experimental resolution which tends to broaden the measured distributions. Instead, the primary differences between the theoretically predicted and measured curves can be attributed to the nonzero duration of the HCP.

Consider a classical atomic electron exposed to a HCP. The energy transferred to the electron is equal to the work done by the HCP, $\Delta E=-\int \vec{F}_{\mathrm{HCP}}(t)\cdot\vec{p}(t)dt$. Ionization occurs if this energy transfer exceeds the electron's initial binding energy $\Delta E > E$. We can write $\vec{p}=\vec{p}_a(t)+\vec{A}(t)+\delta\vec{p}(t)$, where $\vec{p}_a(t)$ is the momentum of the electron in the absence of the HCP, $\vec{A}(t)$ is the partial impulse delivered to a free electron at time t during the pulse, and $\delta\vec{p}(t)$ is an impulse-dependent correction to $\vec{p}_a(t)$. $\delta\vec{p}(t)$ takes into account the difference in the electron's position in the presence of the HCP relative to its position in the absence of the pulse. After performing the integral over the pure impulse term, the ionization condition is

$$E-\frac{1}{2}\vec{A}^2 < -\int \vec{F}_{\mathrm{HCP}}(t)\cdot[\vec{p}_a(t)+\delta\vec{p}(t)]dt, \tag{5}$$

where $\vec{A}$ is the net impulse delivered by the HCP. For a rectangular HCP with constant amplitude for $0 \leqslant t \leqslant \tau_{\mathrm{HCP}}$, Eq. (5) becomes

$$E-\frac{1}{2}\vec{A}^2 < \vec{A}\cdot(\bar{\vec{p}}+\overline{\delta\vec{p}}), \tag{6}$$

where $\bar{\vec{p}}$ and $\overline{\delta\vec{p}}$ are the time-averaged values of $\vec{p}_a(t)$ and $\delta\vec{p}(t)$ during the pulse. For nonrectangular pulses, Eq. (6) remains a good approximation provided the effective duration, $\tau_{\mathrm{HCP}} \ll \tau_K$.

The term $\overline{\delta\vec{p}}$ vanishes as $\tau_{\mathrm{HCP}} \to 0$ or $\vec{A} \to 0$ and is a small correction to the purely atomic momentum contribution for the short ($\tau_{\mathrm{HCP}} \ll \tau_K$) and weak ($A_{\max} \sim \sqrt{2E}$) kicks used in our experiments. If we neglect this higher order term, we recover an ionization condition that is identical in form to that obtained in the instantaneous kick limit [see Eq. (1)]. Specifically, ionization occurs if the component of $\bar{\vec{p}}$ in the direction of the kick exceeds a critical value

$$\bar{p}_c > \left(E-\frac{1}{2}A^2\right)\Big/ A. \tag{7}$$

Accordingly, we can define an average momentum distribution $D(\bar{p})$ in analogy to $D(p)$ from Eq. (2). For real, noninstantaneous HCPs, the IMR method enables the recovery of momentum distributions which approximate $D(\bar{p})$. The similarity between $D(\bar{p})$ and $D(p)$ depends on both the duration of the HCP and the form of the momentum distributions to be measured.

To qualitatively assess how momentum averaging affects the various experimental distributions shown in Fig. 3, we first consider the approximately one-dimensional motion of a classical electron in a Stark atom with a large dipole moment along the z axis. The large-momentum wings of the electron's probability distribution reflect the high-velocity motion of the electron near the nucleus ($r \ll n^2$) where its acceleration has the greatest magnitude. Here, even in the absence of the HCP field, the electron's momentum changes substantially during a time interval τ_{HCP}. For example, an electron moving at high speed away from the nucleus at $t=0$ has a much lower speed at a time, $t=\tau_{\mathrm{HCP}}$ later. In a more extreme situation, an electron moving very rapidly toward the nucleus can pass around the ion core and actually reverse its momentum during the time interval τ_{HCP} [15–17]. In either case, the magnitude of $\bar{p}_z$ can be considerably smaller than the magnitude of the initial momentum p_z. Thus, we expect that in our experimental implementation of the IMR method, probability from the highest-momentum wings of the actual distributions $D(p_z)$ will be aliased to lower momentum in the

recovered distributions $D(\bar{p}_z)$. This is indeed observed in the distributions for the larger dipole moment states shown in Fig. 3.

In Stark atoms with small dipole moments, the electron spends a large fraction of its time with high angular momentum, so very high speed (and highly accelerated) motion near the nucleus is forbidden [29]. Accordingly, the high-momentum wings of the distributions for these states are suppressed in comparison to those for states with larger dipole moments. Thus, as observed, we expect less aliasing of probability from high to low momentum in the recovered distributions. Apparently, $D(\bar{p}_z)$, is an accurate representation of $D(p_z)$ for the small $|k|$ states.

Rather than attempting a precise numerical simulation of the experiment that, if done correctly, would simply reproduce the measured distributions, we utilize an approximate computational method that allows us to better assess the validity of the classical analysis leading to Eq. (7). Specifically, we use a semiclassical approximation to construct an effective wave function $\bar{\psi}(\vec{r})$ whose z-momentum distribution is $D(\bar{p}_z)$. We compare these simulated distributions to the experimental results (see Fig. 3).

Before describing the computational procedure, we note that for a given Stark eigenstate $|E,k\rangle$, an equivalent classical electron positioned at a point (x,z) has a momentum in one of four momentum quadrants $(\pm p_x, \pm p_z)$, each associated with motion toward or away from the nucleus in two distinct orbits. The average momentum of an electron on any of these trajectories can be calculated from the classical equations of motion, by following the electron's trajectory during a time interval τ_{HCP}. We use an analogous procedure to approximate $\bar{\psi}(x,z)$ and $D(\bar{p}_z)$ for a quantum mechanical eigenstate.

First, the stationary wave function for a given initial Stark state is computed on a Cartesian coordinate grid. We note that because of cylindrical symmetry about the z axis, it is only necessary to compute the effective, momentum-averaged wave function in the xz plane. The full three-dimensional wave function $\bar{\psi}(\vec{r})$ can then be constructed from this two-dimensional slice. Next, a Fourier transform filter is used to re-express the stationary wave function in terms of four, orthogonal, component wave functions $\psi(x,z)=\Sigma_{j=1}^{4}\psi_j(x,z)$, each with momentum constrained to one of four momentum quadrants $(+p_x,+p_z)$, $(+p_x,-p_z)$, $(-p_x,+p_z)$, $(-p_x,-p_z)$, for $j=1-4$, respectively. Each grid element within each $\psi_j(x,z)$ is considered to be the starting point of a classical trajectory where the electron's initial momentum is set equal to the expectation value of momentum within that grid element. That initial momentum is used to calculate the position change of the electron during a small time interval. The expectation value of momentum within the grid element corresponding to the electron's new position is then used to find the next point on the trajectory, etc. [30]. The path of the electron is followed over a time interval τ_{HCP} and we compute the time-average phase $\bar{\phi}_j(x,z)$ of the component wave function $\psi_j(x,z)=|\psi_j(x,z)|e^{i\phi_j(x,z)}$ along that path.

The effective wave function $\bar{\psi}(x,z)$ is then obtained using a semiclassical approximation [31]. Specifically, we exploit the fact that the magnitude of each component wave function, $|\psi_j(x,z)|$ is a slowly varying function of position, changing negligibly over distances comparable to the electron DeBroglie wavelength. Thus, the change in the electron's momentum over any trajectory is determined almost entirely by the variation in the wave function phase $\phi(x,z)$. Therefore, we construct effective component wave functions $\bar{\psi}_j(x,z)=|\psi_j(x,z)|e^{i\bar{\phi}_j(x,z)}$ by replacing the the initial wave function phase $\phi_j(x,z)$ with the trajectory averaged phase $\bar{\phi}_j(x,z)$ at each point. Since only the phase of the wave-packet is modified, normalization is precisely maintained. The component wavefunctions $\bar{\psi}_j(x,z)$ are Fourier transformed into momentum space, and their respective z-momentum distributions are added to produce $D(\bar{p}_z)$. The simulated distributions shown in Fig. 3 were obtained assuming $\tau_{\mathrm{HCP}}=500$ fsec, and have been smoothed to the instrumental resolution of the imaging spectrometer ($\sim$0.002 atomic momentum units) to allow more direct comparison with experiment. As expected, for the largest dipole moment states ($k=-26$ and -24 in Fig. 3), probability from the high-momentum wings of the "exact" distributions has been aliased to lower momentum in the simulated and measured distributions. In all cases, the experimental distributions are more accurately reproduced by the simulations than by the "exact" distributions.

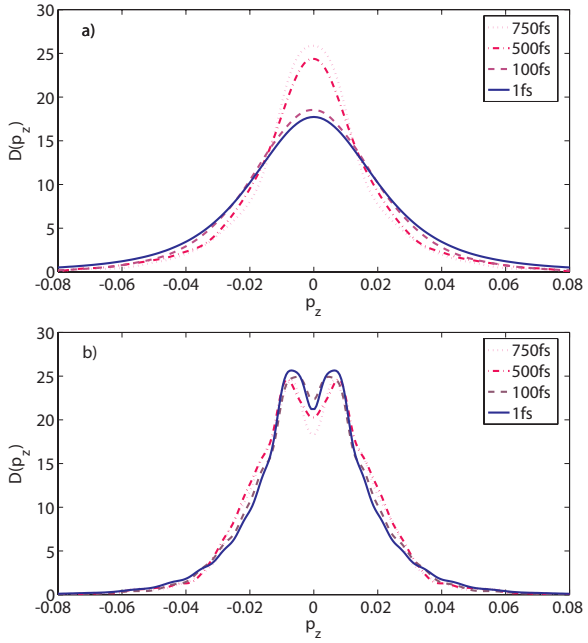

FIG. 4. (Color online) Simulated momentum distribtutions for (a) the $n=28, k=-26$ eigenstate and (b) the $n=28, k=-6$ eigenstate using various HCP durations. For $\tau_{\mathrm{HCP}}=1$ fsec the recovered momentum distribution is indistinguishable from that computed directly from Eq. (3). A 500 fs probing window obtains the best agreement with the measurement, consistent with previous measurements of the HCP duration [22].

Figure 4 shows calculated distributions $D(\bar{p}_z)$ obtained using several different HCP durations, for two different $n=28$

Stark states. For the small dipole moment state, in which the electron has little probability of traveling near the nucleus with high velocity and high acceleration, $D(\bar{p}_z)$ accurately approximates $D(p_z)$ for HCP durations up to 500 fsec or more. However, similar accuracy is only achieved for the large dipole moment state if $\tau_{\mathrm{HCP}} < 100$ fsec.

In summary, we have used an improved impulsive momentum retrieval technique to measure approximate z-momentum distributions of Rydberg electrons in a static electric field. The visibility of predicted fine-structure within the $n=28, k=-6$ distribution confirms the high resolution of the method. We use a classical analysis to show that for HCPs with nonzero durations, the IMR method enables the recovery of the probability distribution for the electronic momentum, time averaged over the HCP duration. We incorporate this notion in a semiclassical calculation to simulate the experimental results. Reasonable agreement between simulated and measured distributions is obtained. The simulations further indicate that this improved AM-IMR method is especially well suited for viewing subtle changes in the time-dependent electron momentum distributions of wavepackets with predominantly higher angular momentum content. Interestingly, these higher angular momentum wavepackets cannot be easily probed using other techniques.

The authors gratefully acknowledge support from the AFOSR and NSF IGERT Program.

[1] R. R. Jones, Phys. Rev. Lett. **76**, 3927 (1996).
[2] C. O. Reinhold, J. Burgdorfer, M. T. Frey, and F. B. Dunning, Phys. Rev. A **54**, R33 (1996).
[3] M. T. Frey, F. B. Dunning, C. O. Reinhold, and J. Burgdorfer, Phys. Rev. A **55**, R865 (1997).
[4] C. Raman, T. C. Weinacht, and P. H. Bucksbaum, Phys. Rev. A **55**, R3995 (1997).
[5] H. Maeda and T. F. Gallagher, Phys. Rev. Lett. **92**, 133004 (2004).
[6] H. Maeda, D. V. L. Norum, and T. F. Gallagher, Science **307**, 1757 (2005).
[7] J. Bromage and C. R. Stroud, Phys. Rev. Lett. **83**, 4963 (1999).
[8] A. Wetzels, A. Gürtler, H. G. Muller, and L. D. Noordam, Eur. Phys. J. D **14**, 157 (2001).
[9] M. B. Campbell, T. J. Bensky, and R. R. Jones, Phys. Rev. A **58**, 514 (1998).
[10] M. B. Campbell, T. J. Bensky, and R. R. Jones, Phys. Rev. A **59**, R4117 (1999).
[11] J. G. Zeibel and R. R. Jones, Phys. Rev. A **68**, 023410 (2003).
[12] F. Robicheaux, Phys. Rev. A **56**, R3358 (1997).
[13] W. Zhao, J. C. Lancaster, F. B. Dunning, C. O. Reinhold, and J. Burgdorfer, Phys. Rev. A **69**, 041401(R) (2004).
[14] A. Wetzels, A. Gurtler, F. Rosca-Pruna, S. Zamith, M. J. J. Vrakking, F. Robicheaux, and W. J. van der Zande, Phys. Rev. A **68**, 041401(R) (2003).
[15] R. R. Jones, N. E. Tielking, D. You, C. S. Raman, and P. H. Bucksbaum, Phys. Rev. A **51**, R2687 (1995).
[16] A. Bugacov, B. Piraux, M. Pont, and R. Shakeshaft, Phys. Rev. A **51**, 4877 (1995).
[17] C. Manescu, J. L. Krause, and K. J. Schafer, Phys. Rev. A **68**, 013405 (2003).
[18] B. Podolsky and L. Pauling, Phys. Rev. **34**, 109 (1929).
[19] H. A. Bethe, and E. E. Salpeter, *Quantum Mechanics of One- and Two-Electron Atoms* (Plenum, New York, 1977).
[20] M. L. Zimmerman, M. G. Littman, M. M. Kash, and D. Kleppner, Phys. Rev. A **20**, 2251 (1979).
[21] D. Park, Z. Phys. **159**, 155 (1960).
[22] D. You, R. R. Jones, D. R. Dykaar, and P. H. Bucksbaum, Opt. Lett. **18**, 290 (1993).
[23] R. R. Jones, D. You, and P. H. Bucksbaum, Phys. Rev. Lett. **70**, 1236 (1993).
[24] M. B. Campbell, T. J. Bensky, and R. R. Jones, Opt. Express **1**, 197 (1997).
[25] R. R. Jones and M. B. Campbell, Phys. Rev. A **61**, 013403 (2000).
[26] N. E. Tielking, T. J. Bensky, and R. R. Jones, Phys. Rev. A **51**, 3370 (1995).
[27] F. Robicheaux, Phys. Rev. A **60**, 431 (1999).
[28] J. Murray-Krezan, PhD. thesis, University of Virginia, Charlottesville, 2006.
[29] T. P. Hezel, C. E. Burkhardt, M. Ciocca, and J. J. Leventhal, Am. J. Phys. **60**, 324 (1991).
[30] If p_x or p_z becomes negligibly small during the time evolution, it indicates that the electron is moving into another momentum quadrant. The computation then continues using a different component wave function $\psi_j(x,z)$ corresponding to the new momentum quadrant.
[31] Harald Friedrich, *Theoretical Atomic Physics* (Springer-Verlag, Berlin, 1990).